Journal of Advanced Research 23 (2020) 123–132

Contents lists available at ScienceDirect

Journal of Advanced Research

journal homepage: www.elsevier.com/locate/jare

Application of robotic-assisted *in situ* 3D printing in cartilage regeneration with HAMA hydrogel: An *in vivo* study

Kaiwei Ma [a,1], Tianzheng Zhao [a,1], Longfei Yang [a], Peng Wang [b], Jing Jin [b], Huajian Teng [b], Dan Xia [a], Liya Zhu [c], Lan Li [b,*], Qing Jiang [b,*], Xingsong Wang [a,*]

[a] *School of Mechanical Engineering, Southeast University, Nanjing, China*
[b] *State Key Laboratory of Pharmaceutical Biotechnology, Department of Sports Medicine and Adult Reconstructive Surgery, Drum Tower Hospital Affiliated to Medical School of Nanjing University, Nanjing, China*
[c] *School of Electrical and Automation Engineering, Nanjing Normal University, Nanjing, China*

GRAPHICAL ABSTRACT

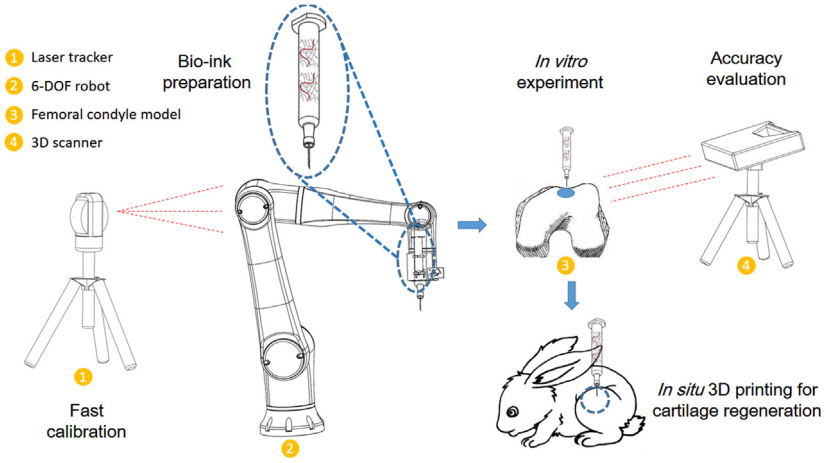

ARTICLE INFO

Article history:
Received 16 November 2019
Revised 5 January 2020
Accepted 21 January 2020
Available online 28 January 2020

Keywords:
In situ 3D bio-printing
Cartilage regeneration
Tissue engineering

ABSTRACT

The concept of *in situ* 3D bio-printing was previously reported, while its realization has still encountered with several difficulties. The present study aimed to report robotic-assisted *in situ* 3D bio-printing technology for cartilage regeneration, and explore its potential in clinical application. A six-degree-of-freedom (6-DOF) robot was introduced in this study, and a fast tool center point (TCP) calibration method was developed to improve printing accuracy. The bio-ink consisted of hyaluronic acid methacrylate and acrylate-terminated 4-armed polyethylene glycol was employed as well. The *in vitro* experiment was performed on a resin model to verify the printing accuracy. The *in vivo* experiment was conducted on rabbits to evaluate the cartilage treatment capability. According to our results, the accuracy of the robot could be notably improved, and the error of printed surface was less than 30 μm. The osteochondral defect could

Peer review under responsibility of Cairo University.

* Corresponding authors at: School of Mechanical Engineering, Southeast University, No.2 Southeast Road, Nanjing 210000, China (X. Wang). State Key Laboratory of Pharmaceutical Biotechnology, Department of Sports Medicine and Adult Reconstructive Surgery, Drum Tower Hospital affiliated to Medical School of Nanjing University, No. 321 Zhongshan Road, Nanjing, China (Q. Jiang and L. Li).

E-mail addresses: lanl17@163.com (L. Li), qingj@nju.edu.cn (Q. Jiang), xswang@seu.edu.cn (X. Wang).

[1] Kaiwei Ma and Tianzheng Zhao contributed equally to this work.

https://doi.org/10.1016/j.jare.2020.01.010
2090-1232/

Bio-ink crosslinking
Robot

be repaired during about 60 s, and the regenerated cartilage in hydrogel implantation and *in situ* 3D bio-printing groups demonstrated the same biomechanical and biochemical performance. We found that the cartilage injury could be treated by using this method. The robotic-assisted *in situ* 3D bio-printing is highly appropriate for improving surgical procedure, as well as promoting cartilage regeneration.

Introduction

Over the past decades, three-dimensional (3D) bio-printing technology has been extensively applied in the field of tissue engineering. To date, several types of 3D bio-printing were developed to fabricate scaffolds for cell culture and tissue regeneration, including stereolithography, inkjet bio-printing, laser-assisted bio-printing, extrusion-based bio-printing, and electrospinning-based bio-printing [1]. Briefly, the process is carried consisting of bio-printing a scaffold *in vitro*, cultivation of cells using bioactive factors for few days or weeks, and finally *in vivo* implantation to repair the damaged region. The whole process typically lasts for a couple of weeks to months. However, the waiting period is a bit long for utilization of 3D bio-printing in clinical treatment. In order to eliminate the existing gap between laboratory and clinical findings in tissue engineering, Campbell and Weiss defined bio-printing as the selective deposition of 'bio-inks' of biologically active components, involving proteins, peptides, DNA, cells, hormones (e.g., cytokines, growth factors, synthetic hormonal signaling peptides, etc.), extracellular matrix (ECM) molecules, and native or synthetic biopolymers. They demonstrated that Bio-printing holds a great promise for tissue engineering, while these technologies are still in relatively early stages of development and have numerous hurdles to overcome [2]. Based on the previous achievements, almost all the elements in 3D bio-printing are obstacle for *in situ* additive manufacturing. For instance, the 3D bio-printing equipment is massive and the working space is small, the crosslinking of bio-inks is difficult in humoral microenvironment, and there is a remarkable uncertainly in accuracy of bio-printing. To overcome these shortcomings, a number of solutions have been recently reported to facilitate the implementation of *in situ* 3D bio-printing technology.

The execution mode of *in situ* 3D bio-printing can be divided into robotic and handheld modes. The robotic mode is similar to the conventional 3D bio-printing technology. The motion of the bio-printing unit is driven by a three-axis portable system, and the printing path is generated using a 3D bio-printing slicer software [3]. The shape of a printing objective depends on the predefined 3D geometry, and complex internal structures can be accordingly obtained. The handheld mode is entirely different from robotic mode, and the bio-printing unit is syringe-like and driven by human. In addition, predefined printing path and geometry are unnecessary, because the shape of a bio-printing objective is completely based on the motion of operator's hand [4]. This mode is highly appropriate for fabrication of simple structures with superficial position and limited damage. The two modes both possess advantages and disadvantages. The robotic mode is highly essential for precise reconstruction of tissues, while that is costly and there are a number of ethical challenges. The handheld mode is easier for sterilization and clinical location, and the ethical challenges can be avoided as well [5]. However, it is difficult to achieve multi-biomaterial 3D bio-printing, restricting its application in the repair of complex tissues.

In 2010, a number of French scholars employed the laser-assisted bio-printing to repair the calvarial defect *in situ*, and they selected nano-hydroxyapatite (n-HA) as the bio-ink [6]. Although the regeneration effect was not reported to be satisfactory, their research was carried out as the first *in vivo* experiment of *in situ* 3D bio-printing. In their next research, mesenchymal stromal cells (MSCs) were utilized in the preparation of bio-ink, in which the bone repairing effect was notably improved [6]. Cohen et al. proposed the concept of the *in situ* repair of cartilage and osteochondral defects using *in situ* additive manufacturing technology, expanding the applications of 3D printing in cartilage tissue engineering [7]. In the mentioned study, a commercial 3D bio-printer was employed to complete the 3D bio-printing process on the calf femur. The alginate and demineralized bone matrix were applied to eliminate the bone defects. The whole of the 3D bio-printing process was completed by a modified commercial 3D bio-printer. Another study reported a satisfied osteochondral repairing effect that was accomplished by a robotic arm-based 3D bio-printer [8]. In addition to bone defects, the skin defects were reported to be repaired *in situ* using multi-nozzle inkjet print-heads driven by the three-axis movement system [9,10]. With presenting the wound scanner, geometry of the defect could be appropriately achieved, and the injured skin could be fully repaired with the bio-ink, which provided a novel solution for early treatment and rapid closure of acute or chronic skin wounds. In contrast to the robotic-assisted 3D bio-printing system mentioned above, a number of Australian scholars focused on the developing *in situ* handheld 3-D bio-printing for cartilage regeneration. They presented a hand-held 3D printing device (BioPen) that allows the simultaneous coaxial extrusion of bioscaffold and cultured cells directly into the cartilage defect *in vivo* in a single-session surgery [4,11]. The co-axial design of the BioPen can fabricate tubular structure with a bio-ink shell [12]. A uniform cell distribution and high cell viability could be accordingly achieved by the BioPen. In their *in vivo* experiment, a standardized critical-sized full-thickness chondral defect was created in the weight-bearing surface of the lateral and medial condyles of both femurs of six sheep. At 8 weeks after surgery, macroscopic, microscopic and biomechanical tests were performed, and it was unveiled that real-time, *in vivo* bio-printing with cells and scaffold is a feasible means of delivering a regenerative medicine strategy in a large animal model to regenerate articular cartilage. The above-mentioned studies demonstrated that the realization of *in situ* 3D bio-printing is highly feasible in clinical practice.

Although some optimistic progresses have been made, numerous difficulties are still existed. In our previous study, we found that the accuracy of 3D bio-printing can meet the requirements of the bone and cartilage repair [13]. However, the limited workspace of a 3D bio-printer restricts the application area, and the damaged region must be placed in the workspace. This issue is the major technical obstacle for the translation of *in situ* 3D bio-printing from benchside to bedside. A robust device for clinical application has mainly two typical sizes: either large enough to wrap the whole body (e.g., computed tomography (CT) or nuclear magnetic resonance (NMR)), or small in size, while large in workspace (e.g., Da Vinci surgical system or MAKOplasty robotic surgery). These two types can easily scan or complete surgery on each patient's position. Considering the occasion and purpose of application, a 3D bio-printer with a large workspace and small size of equipment is highly convenient for surgeons. Herein, we introduced a six-degree-of-freedom (6-DOF) robot to solve the aforementioned

challenge. For this purpose, a fast tool center point (TCP) calibration method was employed to improve the accuracy of 3D bio-printing. Besides, we used hyaluronic acid methacrylate (HAMA) as a bio-ink due to its excellent performance in cartilage regeneration [14,15]. To enhance the mechanical properties and speed of photopolymerization, the acrylate-terminated four-armed polyethylene glycol (4-Armed PEG-ACLT) was introduced in the bio-ink to act as a cross-linker [16,17]. Eventually, an *in vivo* study was conducted on knee joint of a rabbit to verify the practicability of the proposed approach in repair of cartilage. Our approach may enhance *in situ* 3D bio-printing in clinical treatment.

Materials and methods

Synthesis of bio-ink

In the present research, HAMA was synthesized as previously reported [18]. Hyaluronic acid (HA) modified with a double-bond was synthesized by reacting with the methacrylic acid (MA). In addition, 2 g HA was dissolved in 100 mL distilled (DI) water, and then, stirred in a cold room overnight, which followed by addition of 1.6 mL MA into the HA solution. The pH of the reaction was maintained between 8 and 9 by addition of 5 N NaOH and kept at 4 °C under continuous stirring for 24 h. Subsequently, HAMA was precipitated in acetone, washed with ethanol, and then dissolved in deionized water (DI) water. After doing dialysis against DI water for 48 h, the purified HAMA with a yield of 87.5% was obtained by lyophilization. The purified HAMA and 4-Armed PEG-ACLT were dissolved in the phosphate-buffered saline (PBS) solution to a final concentration of 2% w/v and 5% w/v before 3D bio-printing. The 4-Armed PEG-ACLT was purchased from Sinopec Shanghai Petrochemical Co., Ltd. (Shanghai, China), and other regents were purchased from Sigma-Aldrich (St. Louis, MO, USA).

Fabrication of robotic-assisted 3D bio-printing system

The robotic-assisted 3D bio-printing system was consisted of a 6-DOF robot, an extrusion-based bio-printing unit, an air compressor, a control cabinet, and a workbench (Figure S1). The robot had a reach of 1 m and handling capacity of 10 kg, which fully met the requirement of 3D bio-printing. According to the functions provided by the robot, we developed an off-line programming software for this system. The main interface is shown in Figure S2. In the developed software, the relevant 3D bio-printing parameters (e.g., diameter of nozzle, speed of printing, etc.) were set to generate the bio-printing process. The program was also debugged in the non-print mode to improve the bio-printing process.

The workspace of the robot was computed by the Monte Carlo method. The limited value of each joint angle was imported into the MATLAB 2016 software (MathWorks, Natick, MA, USA) to generate the random values of the joint angle using the Rand (N, 1) function. A total of 6 groups of numerical values (30000 values for each group) were substituted into the kinematic equation of the robot in an order, in which they were generated to obtain the end effector relative to the base coordinate system.

Fast calibration of the 3D bio-printing system

A traditional robot calibration technology requires expensive and complicated equipment, thus some calibration methods have been developed that only adopt internal encoder data of a robot. Briefly, in the current study, the robot was set to touch a number of special points using TCP, and the touch accuracy was judged by human eyes, which resulted in a large error in the calibration process. Thus, we utilized a fast calibration method in the present study. The calibration method accurately calculated the TCP according to the kinematic model of the robot, the distance constraints, and the measurement of the laser tracker. It was unveiled that the calibration error was reduced by the proposed approach.

The kinematic model of the robot was established using the D-H method [19], and the coordinate systems were set as illustrated in Fig. 1.

where a_i represents the length of link, α_i denotes the link twist, d_i is the link offset, and θ_i represents the joint angle. The link-based parameters are presented in Table S1.

According to the coordinate systems and the link-based parameters, the relationship between adjacent coordinate systems is given by

$$ {}^{i-1}_{i}T = \begin{bmatrix} \cos\theta_i & -\sin\theta_i\cos\alpha_i & \sin\theta_i\sin\alpha_i & a_i\cos\theta_i \\ \sin\theta_i & \cos\theta_i\cos\alpha_i & -\cos\theta_i\sin\alpha_i & a_i\sin\theta_i \\ 0 & \sin\alpha_i & \cos\alpha_i & d_i \\ 0 & 0 & 0 & 1 \end{bmatrix} \quad (1) $$

Then, the kinematic model of the robot is formulated as

$$ {}^{0}_{6}T = \prod_{i=1}^{6} {}^{i-1}_{i}T \quad (2) $$

where ${}^{0}_{6}T$ represents the transformation equation from {0} to {6}.

Based on the coordinate systems for calibration (Figure S3), {B} is the base coordinate system of the robot, {E} represents the coordinate system of the flange at the end of the robot, {L} is the coordinate system of the laser tracker, and C denotes the center point of the target ball. According to Eqs. (1–2), Eq. (3) is given by

$$ {}^{B}_{E}T = {}^{0}_{6}T \quad (3) $$

where ${}^{B}_{E}T$ is the transformation matrix from {B} to {E}.

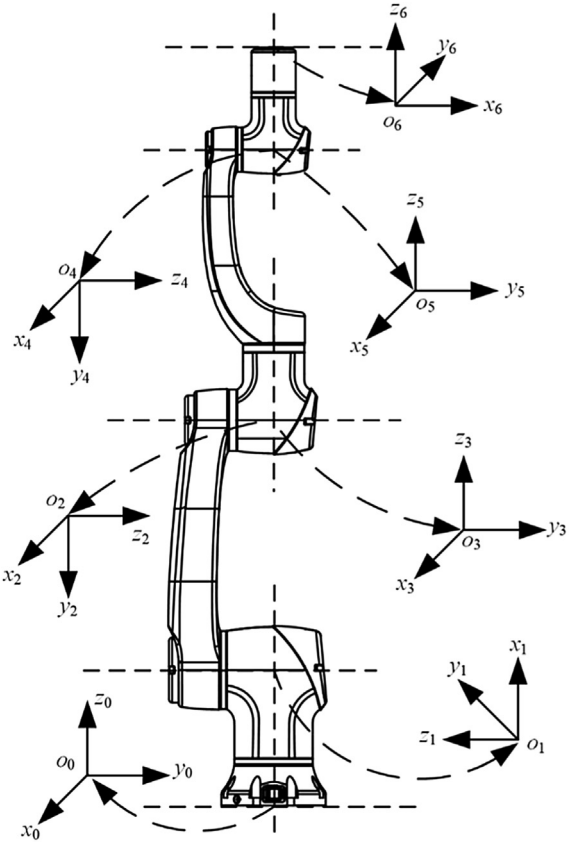

Fig. 1. The coordinate systems of the 6-DOF robot.

The position of point C can be written as

$$ {}^{E}P = \begin{bmatrix} {}^{E}P_x & {}^{E}P_y & {}^{E}P_z & 1 \end{bmatrix}^{T} \tag{4} $$

where ${}^{E}P$ denotes the transformation matrix from $\{E\}$ to C, and $({}^{E}P_x, {}^{E}P_y, {}^{E}P_z)$ represents the coordinate value of C in $\{E\}$.

At this point, C can be represented in $\{B\}$ as

$$ {}^{B}T_C = {}^{B}_{E}T_C \cdot {}^{E}P \tag{5} $$

where ${}^{B}T_C$ denotes the transformation equation from $\{B\}$ to C, and ${}^{B}_{E}T_C$ is the matrix obtained by substituting the link-based parameters of point C into Eq. (3).

As mentioned above, it can be concluded that ${}^{E}P_x$, ${}^{E}P_y$ and ${}^{E}P_z$ are unknown parameters that require solutions. If two different measuring positions M and N are chosen arbitrarily, the difference between the two points is calculated as follows:

$$ \Delta {}^{B}P_{MN} = {}^{B}T_M - {}^{B}T_N = EBT_M \cdot {}^{E}P - EBT_N \cdot {}^{E}P \tag{6} $$

where $\Delta {}^{B}P_{MN}$ is the difference between the coordinates of the two points M and N in $\{B\}$, ${}^{B}T_M$ and ${}^{B}T_N$ are the transformation equations from $\{B\}$ to M and N, respectively, ${}^{B}_{E}T_M$ and ${}^{B}_{E}T_N$ are the matrices obtained by substituting the link-based parameters of M and N into Eq. (3), respectively.

Simultaneously, the position of the two points measured by the laser tracker is

$$ \Delta {}^{L}P_{MN} = {}^{L}T_M - {}^{L}T_N \tag{7} $$

where $\Delta {}^{L}P_{MN}$ is the difference between the coordinates of the two points M and N in $\{L\}$, and ${}^{L}T_M$ and ${}^{L}T_N$ are the transformation matrices from $\{L\}$ to M and N, respectively.

Although the coordinate values of the points in $\{B\}$ and $\{L\}$ are different, the distance between M and N in the two coordinate systems is equal, that is

$$ \| \Delta {}^{B}P_{MN} \| = \| \Delta {}^{L}P_{MN} \| \tag{8} $$

It can be written as

$$ \| {}^{B}_{E}T_M \cdot {}^{E}P - {}^{B}_{E}T_N \cdot {}^{E}P \| = \| {}^{L}T_M - {}^{L}T_N \| \tag{9} $$

In Eq. (9), ${}^{B}_{E}T_M$ and ${}^{B}_{E}T_M$ can be calculated by the link-based parameters corresponding to points M and N, respectively. ${}^{L}T_M$ and ${}^{L}T_N$ are obtained by the laser tracker. Thus, the three unknown parameters contained in ${}^{E}P$ require solutions for the calibration. Besides, any two points in the space can formulate an equation according to Eq. (9). Therefore, at least three points are required to complete the calibration. We used the laser tracker to collect six points and the control cabinet to record the link-based parameters of the points. Consequently, three equations were formulated, and were solved to obtain ${}^{E}P$. Eventually, the reference TCP value (-88.6049, 105.9695, 90.9429) was achieved.

According to the geometric size and the reference TCP value, the TCP value of the nozzle was computed by the off-line programming software.

In order to verify accuracy of calibration for TCP, the transformation matrix ${}^{L}_{B}T$ from $\{L\}$ to $\{B\}$ was calculated. Theoretically, C in $\{L\}$ can be expressed as

$$ {}^{L}T_C = {}^{L}_{B}T_L \cdot {}^{B}T_C = {}^{L}_{B}T_L \cdot {}^{B}_{E}T_C \cdot {}^{E}P \tag{10} $$

where ${}^{L}T_C$ represents the coordinate value of C in $\{L\}$.

In the solution of ${}^{L}_{B}T_L$, ${}^{L}T_C$ could be obtained by laser tracker, and ${}^{B}T_C$ could be calculated by Eq. (5). Using ${}^{L}T_C = {}^{L}_{B}T_L \cdot {}^{B}T_C$ and four measuring points, the non-homogeneous linear equations with twelve unknowns could be formulated, and then, ${}^{L}_{B}T$ was attained.

In the analysis of accuracy of TCP, we selected ${}^{L}T_C = {}^{L}_{B}T_L \cdot {}^{B}_{E}T_C \cdot {}^{E}P$ in Eq. (10). At this time, ${}^{L}_{B}T$ and ${}^{B}_{E}T_C$ were found as known numbers. The theoretical value of ${}^{L}T_C$ was achieved by substituting the TCP value obtained by the fast calibration method into ${}^{E}P$. The actual value of ${}^{L}T_C$ was obtained by the laser tracker. By subtracting these two values, the accuracy of the fast TCP calibration method was calculated. Analogously, the accuracy of the traditional TCP calibration method could be obtained by substituting ${}^{E}P$ in the traditional TCP calibration method into the equation.

The 3D bio-printing path planning

Herein, the 3D bio-printing target was taken as a cylinder into account, and the printing path was designed to fill this specific geometry. The coordinate system was set in the target. As illustrated in Figure S4a, point A and point B represent the positions of 3D bio-printing nozzle, and point C shows any point in the bottom.

The center of the user coordinate system U was set as $U = [U_x, U_y, U_z]$, where U_z could be obtained from the point C, which meant that the Z coordinate of point C in the coordinate system $\{B\}$ was U_z. Besides, U_x and U_y were calculated by the relationship between point A and point B using the following equation

$$ \begin{cases} (U_x - x_A)^2 + (U_y - y_A)^2 = (R - r)^2 \\ (U_x - x_B)^2 + (U_y - y_B)^2 = (R - r)^2 \end{cases} \tag{11} $$

where (x_A, y_A) and (x_B, y_B) denote the coordinate values of X-axis and Y-axis for point A and point B in the coordinate system $\{B\}$, respectively. R represents the radius of the defect, and r is the radius of the 3D bio-printing nozzle.

Then, the origin position of the user coordinate system could be achieved. The orientation of each axis of user coordinate system was the same as $\{B\}$.

After the establishment of the user coordinate system, the bio-printing path was planned based on the parametric line method, and the diagram of the path is schematically shown in Figure S4b. In this algorithm, the user coordinate system was set as the coordinate system of path planning, and the number of vertical lines N in the trajectory could be calculated by Eq. (12).

$$ N = 2n + 1 = 2 \cdot \left[\frac{R - r}{2r} \right] + 1 \tag{12} $$

The abscissa sequence $V(x)$ of each target point could be generated as

$$ V(x) = \{-n \cdot 2r, -(n-1) \cdot 2r, \cdots, 0, \cdots, (n-1) \cdot 2r, n \cdot 2r\}_N \tag{13} $$

The ordinate of each vertical line could be attained by Eq. (14),

$$ y(x) = \pm \sqrt{(R - r)^2 - V(x)^2} \tag{14} $$

where the positive (negative) of $y(x)$ represents the target point of the vertical line that is above (below) the X-axis.

The number of printed layers is given by

$$ T = \left[\frac{H}{2r} \right] \tag{15} $$

where H denotes the height of the damaged region.

Then, the coordinate sequence of Z-axis can be obtained as follows

$$ W = \{2r, 2r \cdot 2, \cdots, 2r \cdot T\}_T \tag{16} $$

According to Eqs. (12)–(16), the coordinate value of each target point can be calculated. With connecting the points with straight lines, then, the desired 3D bio-printing path could be generated.

In vitro experiment

To verify the validity of the 3D bio-printing path, an *in vitro* experiment was performed on a resin femoral condyle model. The model was established with the help of micro CT images of a 6-month-old female New Zealand rabbit, and fabricated using a digital light processing (DLP) 3D bio-printer (Prism, Shanghai, China). A cylinder defect with a diameter of 5 mm and a height of 4 mm was made on the model to mimic an osteochondral injury.

The defect was printed using the robotic-assisted *in situ* 3D bio-printing method with the bio-ink. A 3D scanner (Shining 3D Tech Co., Ltd., Hangzhou, China) was employed to obtain the post-printed geometry. A "3D Samples Comparison" operation was conducted using the Geomagic Control software (3D Systems Inc., Rock Hill, SC, USA) to evaluate the accuracy of bio-printing as described previously [8,13]. The robot calibrated using a traditional method was considered as control group in the current test.

In vivo experiment

The *in vivo* test was performed on female New Zealand rabbits. The animal study was carried out in compliance with the regulations and guidelines of the Ethics Committee of Drum Tower Hospital affiliated to the Medical School of Nanjing University (Nanjing, China), and conducted according to the Institutional Animal Care and Use Committee (IACUC) guidelines.

A total of 12 rabbits (body weight, 2.5 kg) were enrolled in this study and randomly divided into 3 groups, including control group, hydrogel implantation group, and *in situ* bio-printing group. A lateral para-patellar incision was made on the articular surface, and an osteochondral defect with a height of 4 mm and a diameter of 5 mm was made in the center of the trochlear groove. The defects in the *in situ* bio-printing group were directly repaired through the 6-DOF robot using the bio-ink; the defects in the hydrogel implantation group were implanted; and the defects in the control group remained blank. Cefuroxime sodium was injected intramuscularly for 3 days after operation to avoid infection. All animals were post-operatively sacrificed at week 12 to evaluate the chondrogenic capacity.

The surface of the defective region was assessed according to color, integrity, contour, and smoothness, and the repair quality was consequently recorded. The International Cartilage Repair Society (ICRS) macroscopic scoring system was used to assess the macroscopic appearance of the repaired tissue, and the scoring criteria are presented in Table S2 [20].

The biomechanical properties of the regenerated region and the correlated healthy part were evaluated using a nanoindenter (Nanomechanics, Oak Ridge, TN, USA) according to a previous study [21]. The force was set at 1.5 mN, which maintained as long as 5 s after reaching the maximum loading force, and then removed to reach the recovery curve. Each sample had 5 indentation test points.

The surface tomography of the regenerated cartilage and healthy cartilage was observed using a scanning electron microscope (SEM; Hitachi, Tokyo, Japan). After nanoindentation testing, the samples were dehydrated using ethanol solution and freeze-dried. Finally, they were sputter-coated with platinum and imaged with SEM.

The samples for biochemical testing were fixed in 10% formalin for 24 h, and then decalcified in 15% ethylenediaminetetraacetic acid (EDTA) for 28 days. The samples were then embedded into paraffin and cut into 5 μm thick sections. The sections were then stained with toluidine blue, Safranin O, and collagen II. All the sections were observed using a microscope equipped with a charge-coupled device (CCD) camera (Olympus, Tokyo, Japan). The histological results were assessed using the O'Driscoll scoring system [22]. The scoring criteria are shown in Table S3.

Statistical analysis

The macroscopic and histological results were analyzed by 3 investigators who were blinded to the groups. The statistical analysis and exponential curve fitting were performed using SPSS 19.0 software (IBM, Armonk, NY, USA) and Igor Pro 6.12 software (WaveMetrics Inc., OR, USA). Data were presented as mean ± standard deviation, and evaluated using an unpaired Student's *t*-test. P less than 0.05 was considered statistically significant.

Results

Accuracy of the 6-DOF robot

After the calibration process was completed, 16 points were selected as the measurement objects. The results of the movement error are depicted in Fig. 2. Compared with traditional calibration method, the fast TCP calibration method notably reduced the volatility of curves in all axes. The average errors of position accuracy for the X, Y, and Z axes in traditional calibration method were 0.0224 ± 0.5009, 0.1574 ± 0.6900, and -0.2626 ± 0.6144 mm, respectively. These values were decreased respectively to -0.0089 ± 0.1702, 0.0025 ± 0.2773, and -0.0128 ± 0.2143 mm using the fast TCP calibration method. The runout values (subtraction of minimum error from maximum error) of various axes were reduced from 1.6747, 2.0578, and 1.8771 mm to 0.6380, 0.8108, and 0.6538 mm, respectively. The average movement error of these points decreased from 1.050 ± 0.1525 mm to 0.3719 ± 0.0226 mm, indicating improved accuracy and stability of the robot.

The workspace of the 6-DOF robot is displayed in Figure S5. It could reach a maximum distance of 1.188 m and a maximum height of 1.454 m.

Evaluating the feasibility of *in situ* 3D bio-printing

Next, we quantitatively measured the bio-printing accuracy *in vitro* once the fast TCP calibration and path planning were conducted. The whole process is shown in Figure S6. The air pressure applied in the present study was 0.2 MPa, the speed was set to 6 mm/s, the thickness of layer was 320 μm, and the diameter of the nozzle was 400 μm. It was revealed that the defect region was filled by the bio-ink according to the pre-defined bio-printing path. The general view from three directions unveiled that the objective fabricated by *in situ* 3D bio-printing could match the geometry of defect area. To further explore the accuracy of *in situ* 3D bio-printing, the "3D Sample Comparison"was used and the results are illustrated in Fig. 3. The colors on the surface were corresponding to the error magnitude, which meant that the 3D error gradually increased in positive direction as the color transferred from green to red, and gradually increased in negative direction as the color transferred from green to deep blue.

As shown in Fig. 3a, the bio-printed area in control group (traditional calibration) was mainly covered by blue (11.5770 mm^2), and the green and yellow areas were 4.0180 and 2.5470 mm^2, respectively. The distribution of color was changed in Fig. 3b, in which the green area was notably increased to 9.8820 mm^2, and the blue and yellow areas were 3.9970 mm^2 and 4.2120 mm^2, respectively. This phenomenon demonstrated that the most of the surface geometry can completely fit that of the healthy cartilage. The statistical results presented in Table 1 confirmed this conclusion as well. With the help of the fast TCP calibration method, the average error was significantly decreased and the majority of

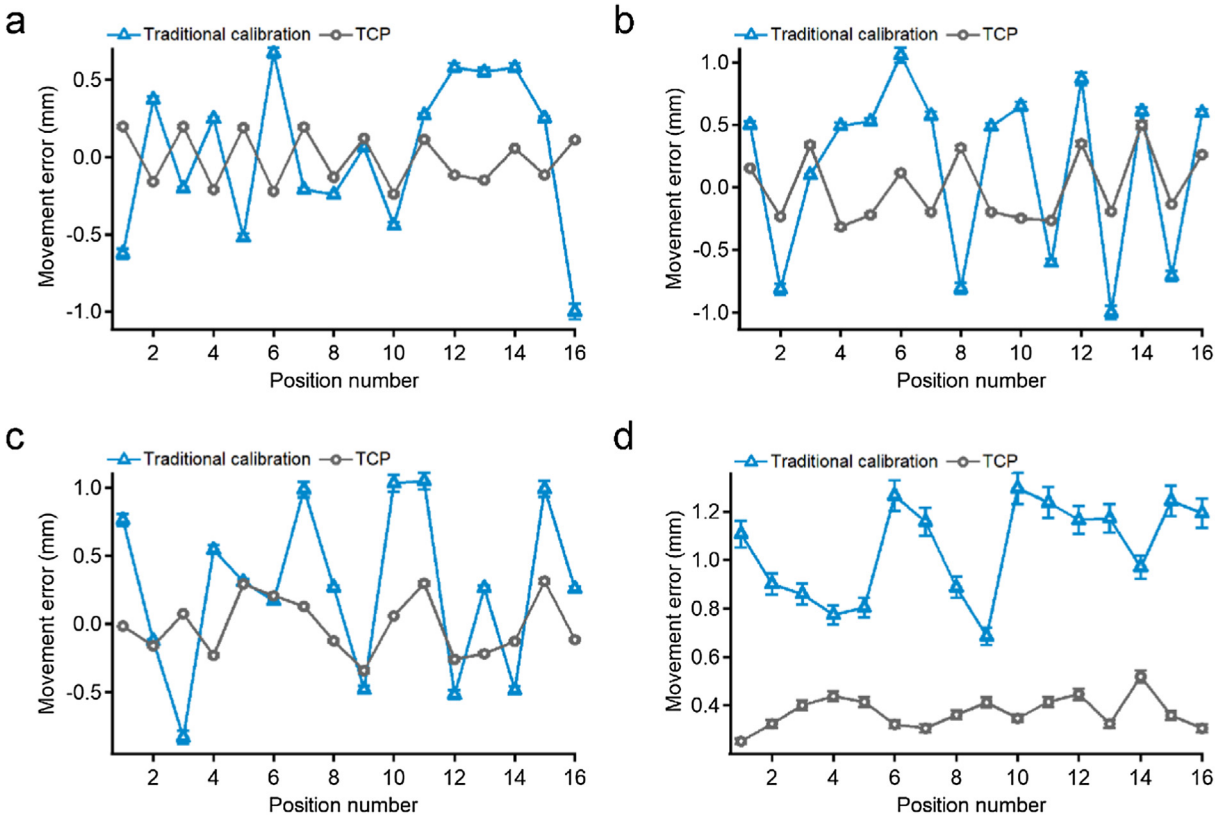

Fig. 2. The movement error of (a) X-axis, (b) Y-axis, and (c) Z-axis. (d) The average coordinate errors of the points.

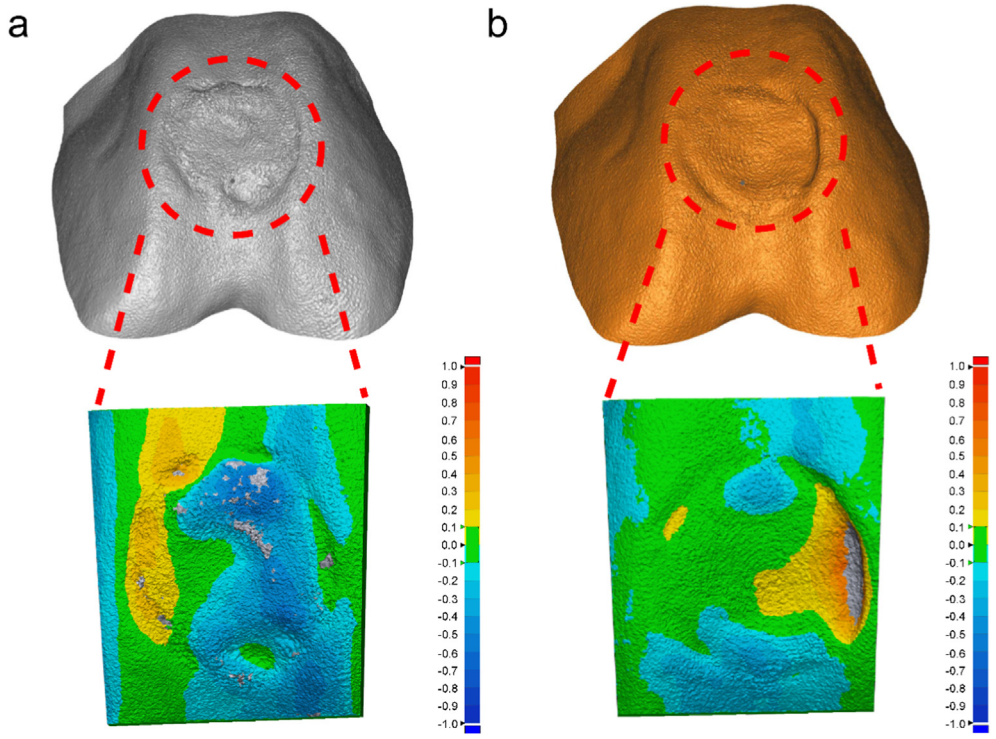

Fig. 3. Comparing the results of (a) traditional calibration and (b) fast TCP calibration.

Table 1
The results of "3D Sample Comparison". *P less than 0.05.

Calibration Method	Average (mm)	Standard deviation (mm)	Dispersion	Within tolerance (%)
Traditional	−0.1550	0.1704	0.0291	30.4617
Fast TCP	−0.0292*	0.1447	0.0209	54.4188*

the points were in the tolerance interval, and the dispersion was also decreased. Thus, it can be concluded that the stability and accuracy of 6-DOF robot are highly appropriate for *in situ* 3D bio-printing, and the effect of bio-printing path plan is accordingly satisfactory.

In situ 3D bio-printing for cartilage regeneration

Finally, we explored the effects of direct *in situ* 3D bio-printing on living animals to evaluate its treatment efficacy. The bio-printing parameters were the same as to those in the *in vitro* experiment (Fig. 4). The osteochondral defect (ICRS grade IV) was made by mosaicplasty. The bio-printing nozzle was dragged to the starting point of the bio-printing path, and the *in situ* 3D bio-printing was carried out according to the planned path. Due to the effects of ultraviolet (UV) light on the camera, the light was turned off during video and photograph shootings, and the photopolymerization was undertaken at the end of the direct bio-printing procedure. The whole process was completed during 60 s, and the experiment was repeated for three times to verify its feasibility.

All the samples were postoperatively harvested for 12 weeks. The surface tomography in healthy group, implantation group, and *in situ* bio-printing group was similar according to the SEM images (Figure S7a). Those images all exhibited a smooth appearance. The biomechanical test demonstrated that the mechanical properties in implantation group and *in situ* bio-printing group were similar, which were lower in both groups than those in the normal cartilage (Figure S7b). The Young's modulus for these three aforementioned groups was 10.0216 ± 1.0601, 6.5859 ± 0.8391, and 6.9115 ± 0.8380 GPa, respectively (Figure S7c).

The gross view in blank control group, hydrogel implantation group, and *in situ* bio-printing group is illustrated in Fig. 5a. It was disclosed that the cartilage defects were repaired in the hydrogel implantation group and *in situ* bio-printing group. The newly-born region in control group was irregular and pale. Compared with blank control group, the regenerated tissue in these two groups exhibited glossy and smooth appearance, which was found similar to native cartilage.

The results of ICRS scoring system are displayed in Fig. 5b, in which the hydrogel implantation group and *in situ* bio-printing group represented approximate points in all items. The score in control group was significantly lower than that in other two groups.

The histological results are presented in Fig. 6a–c. The regenerated tissue in control group did not fill the defect region, and an obvious gap could be observed in this area. In hydrogel implantation group and *in situ* bio-printing group, the defects were fully filled by newly-born tissue. The surface was uniform and smooth. In addition, ECM showed a strong staining with toluidine blue and Safranin O, indicating that the main component was glycosaminoglycan (GAG). The immunohistochemistry unveiled the existence of collagen II in ECM. It was noted that the regenerated tissue in hydrogel implantation group and *in situ* bio-printing group was hyaline cartilage. As depicted in Figure S8, the arrangement of chondrocytes in hydrogel implantation group and *in situ* bio-printing group was closer to native cartilage. They arranged in parallel on the surface layer, and the vertical cells were found in the deep layer, while the cell arrangement in control group was disorganized.

The O'Driscoll scoring system confirmed this conclusion as well (Fig. 6d), in which the rate in hydrogel implantation group and *in situ* bio-printing group was significantly higher than that in control group. Both groups outperformed in cellular morphology, Safranin O staining, structural integrity, cartilage thickness, and cellularity. However, no significant difference was found between these two groups, which was the same as the results of biomechanical test and ICRS scoring system.

Discussion

It is noteworthy that 3D bio-printing technology is highly appropriate, accompanying by a strong potential for the regeneration of complex tissues and organs. However, the realization of this technology still requires further exploration. We, in the present study, used the robotic-assisted 3D bio-printing to repair ICRS grade IV cartilage defects in living animals. To the best of our knowledge, we, for the first time, applied this technology *in vivo*. By introducing a 6-DOF robot, we could achieve a larger workspace as well as satisfied printing accuracy. The bio-ink could quickly react through the irradiation of UV light in the defect region. More importantly, the therapeutic efficacy was remarkable. The biomechanical and biochemical features in *in situ* bio-printing group

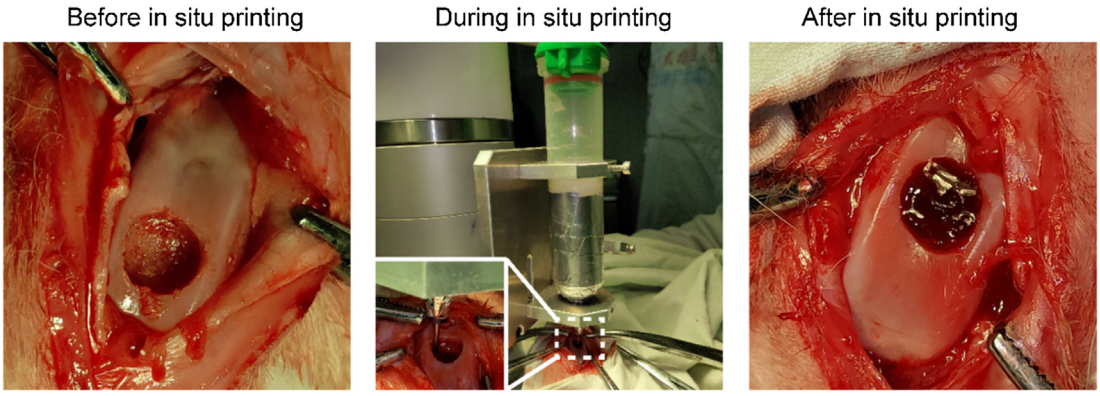

Fig. 4. The process of *in situ* 3D bio-printing applied on knee joint of a rabbit.

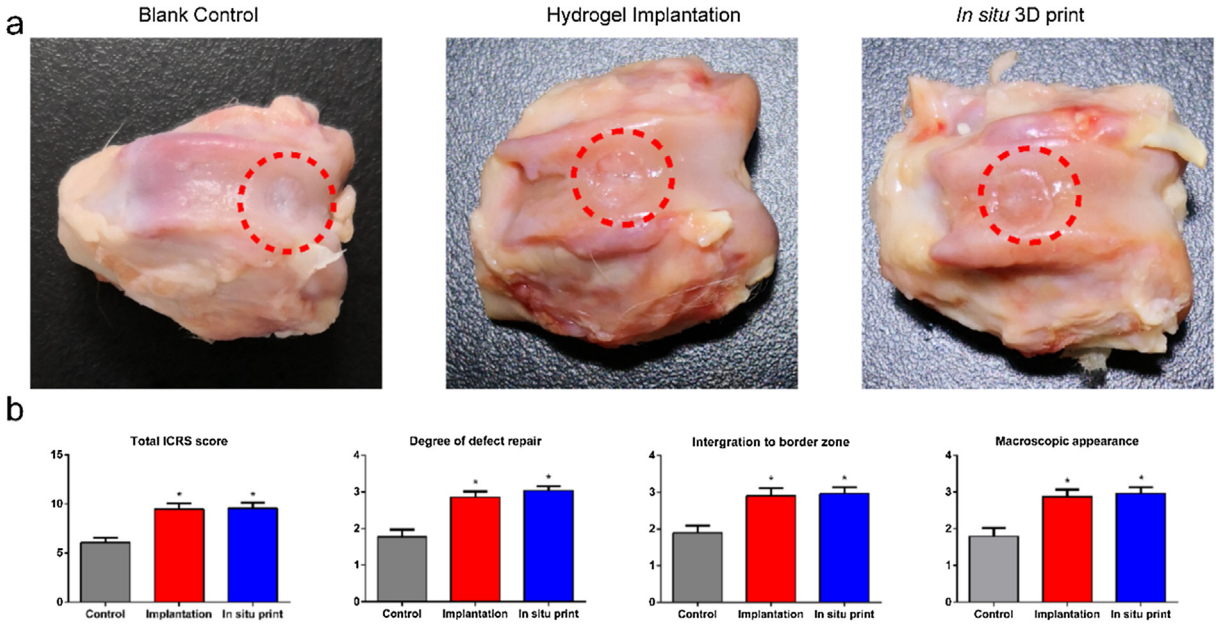

Fig. 5. (a) The gloss view in three groups. (b) The total ICRS score and its detailed items.

and hydrogel implantation group were similar, indicating that the process of fabricating hydrogel *in vitro* can be omitted under certain conditions. Our results suggested that the *in situ* 3D bio-printing technology is highly appropriate to repair injuries, which can directly obtain autogenous MSCs from surrounding microenvironment (e.g., bone and cartilage damage).

Traditional non-surgical therapeutic methods for cartilage injuries include non-steroidal anti-inflammatory drugs (NSAIDs) and opioids [23]. The intra-articular injection and surgery, including mosaic arthroplasty and joint replacement, are highly efficient for patients with severe symptoms that cannot attain adequate pain relief and functional improvement using non-surgical treatments [24]. In the present study, a modified surgical procedure was adopted for mosaic arthroplasty, which was taken as a well-established surgical treatment into account for focal chondral and osteochondral defects [25]. The defect region should be remodeled to the cylinder shape for the purpose of filling graft plugs harvested from non-weight-bearing areas. The geometry of the transplanted plug is highly vital for the successfulness of this surgery [26]. Except for these early complications mentioned above, the late degradation of grafts is another reason for the implantation failure [27].

Thus, *in situ* 3D bio-printing technology is highly appropriate for such risk factors. Firstly, geometry of surgical area is of great importance for execution of 3D bio-printing technology. No extra supporting structures are required for the bio-printing target due to the flat bottom in the defect. The size and curvature of the defect region can be determined according to imaging examinations, including magnetic resonance imaging (MRI) and CT. In addition, 3D scanning is another option to achieve the geometry of defect region. Based on our previous study, the handheld 3D scanner can obtain the required 3D models in a short period of time. We also previously found that resolution (~5 μm) was sufficient for reestablishing the superficial zone, and had only about 200 μm of thickness, which was almost impossible to repair manually [13]. These specific conditions ensured the practicability of the *in situ* 3D bio-printing. In the present study, *in vitro* and *in vivo* experiments mimicked the operative environment of mosaic arthroplasty. The surface error was found to be lower than 30 μm, which was remarkably higher than the accuracy of manual operation.

Secondly, the accuracy of bio-printing can be easily ameliorated by the TCP calibration method. Compared with traditional ball-bar instrument, the fast TCP calibration demonstrated a noticeable improvement in measuring space and operation process [28]. The points used for measurement can be arbitrary in space, and the calibration can be completed as soon as the positions of the points are read. The whole procedure can be accomplished by nonprofessionals, including physicians and nurses. In addition, the computation load of the above-mentioned method is small due to the simply procedure and calibration algorithm. A complex calibration principle generally results in sophisticated calibration algorithm, and the accuracy may decrease in each step of the operation process [29]. Meanwhile, that sophisticated method may be extremely time-consuming and has poor calibration efficiency. However, the proposed fast calibration method can be applied to a robotic-assisted 3D bio-printer with multiple printing units. The required TCP for each bio-printing unit can be automatically generated after the key geometric data can be imported into the software. Using the proposed calibration method, the movement accuracy of the 6-DOF robot used in the present study was increased. The whole calibration process could be completed in 10 min as well.

Finally, it should be noted that massive bleeding in the defect region generally leads to dilution of bio-ink, causing difficulty in terms of adhesion and polymerization, as well as hydrogel swelling and bulging due to damaged region. In contrast to microfracture surgery, the amount of haemorrhage in the mosaic arthroplasty is typically insignificant, which is highly proper for the crosslinking of bio-ink. The bio-ink in the current study consisted of HAMA and 4-Armed PEG-ACLT, which could provide both ECM-like components and acceptable biomechanical properties. The HAMA contains GAG, which can dissipate energy during the load bearing process by adjusting for the included water content [30]. The HA can lubricate cells, regulate cell movement on the viscoelastic matrix, stabilize reticular fibers, and also protect the cells from mechanical damages [31]. The 4-Armed PEG-ACLT was served as the covalent cross-linkers, and the photopolymerization rate of HAMA could be improved in the present research. It generally

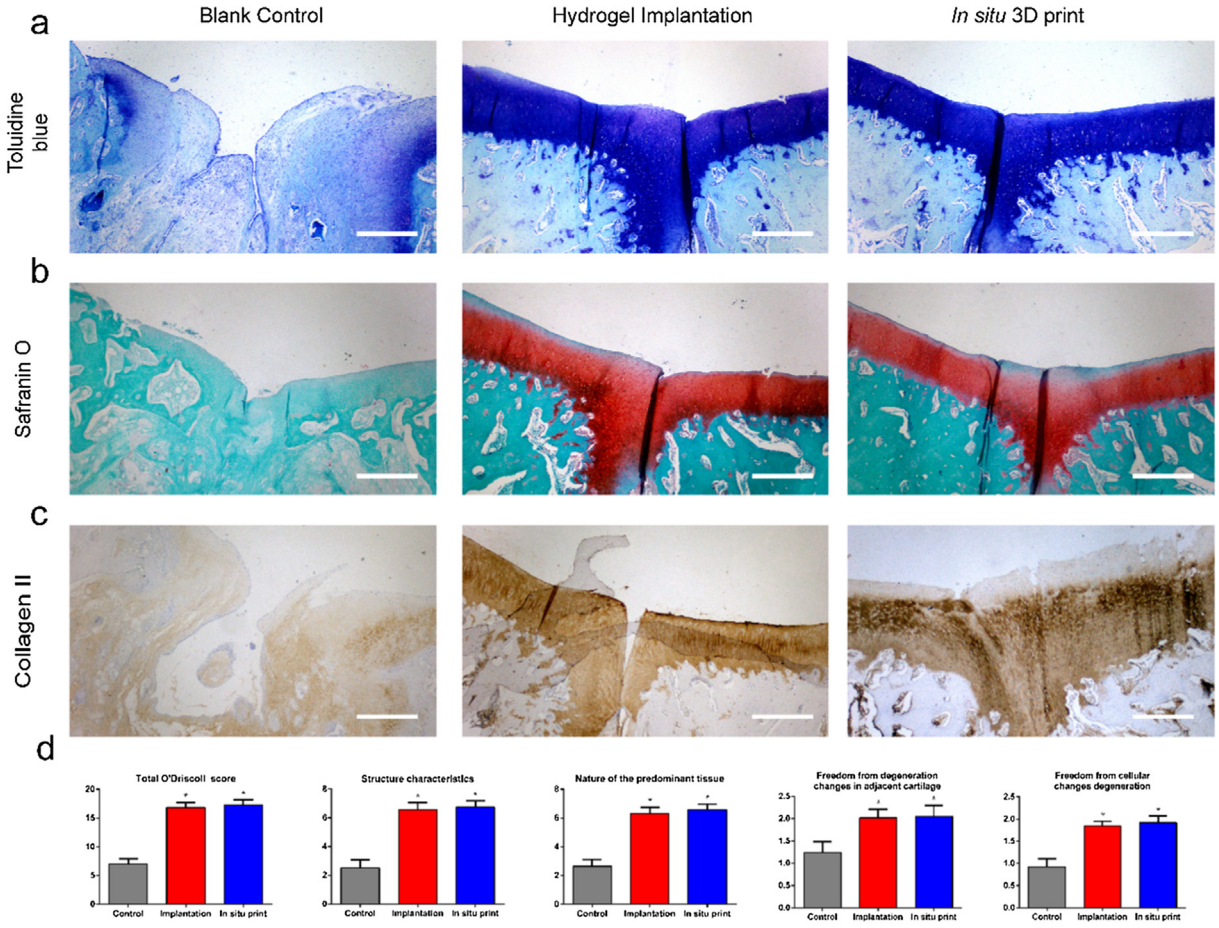

Fig. 6. (a) The toluidine blue staining, (b) safranin O staining, and (c) collagen II staining of each group (Scale bar: 500 μm); (d) The total O'Driscoll score and its detailed items. (For interpretation of the references to color in this figure legend, the reader is referred to the web version of this article.)

improves the mechanical properties due to the higher crosslinking efficiency and density [16]. A fast crosslinking reaction can be accomplished in the defect region during the 3D bio-printing process. Although the bio-ink was cell/drug-free, it could induce the regeneration of hyaline-like cartilage in the injured area. However, the biomechanical properties of the regenerated cartilage were lower than the native cartilage, and an obvious regenerated area could be observed in the center of the defect region. However, the microstructure and the components were the same as native cartilage, indicating that a remarkable improvement space was existed for the bio-ink. The addition of bioactive factors into bio-ink may ameliorate the mechanical properties and the treatment efficacy as well.

Therefore, the *in situ* 3D bio-printing technology can improve the surgical procedure for cartilage injury. Due to the limitation of donation region, the size of mosaic arthroplasty is generally limited to less than 4 cm^2 [32]. Large size of cartilage defect typically requires more than one surgical region, indicating severe trauma in the non-weight-bearing areas. The application of *in situ* 3D bio-printing technology can also decrease the damage in knee joint and increase the graft accuracy.

Conclusions

In the present study, we employed a 6-DOF robot to act as a 3D bio-printer to achieve *in situ* 3D bio-printing. A fast TCP calibration method was developed for improving the robot's movement and bio-printing accuracy. After performing *in vitro* experiment, the *in situ* 3D bio-printing process was conducted on rabbits to repair the ICRS grade IV cartilage defect. The bio-ink could fill the defect region with appropriate geometry and the cartilage injury could be repaired after 12 weeks. This study indicated the feasibility of the mentioned technology for clinical application.

Declaration of Competing Interest

The authors declare that they have no known competing financial interests or personal relationships that could have appeared to influence the work reported in this paper.

Acknowledgments

This study was supported by the National Natural Science Foundation of China (Grant Nos. 51705259, 81420108021, 81730067, 81802135, and 51875101), National Key Research and Development Project (Grant No. 2018YFF0301100), Postgraduate Research & Practice Innovation Program of Jiangsu Province (Grant No. KYCX18_0065), the Key Research and Development Project of Jiangsu Province (Grant No. BE2018010-3), Jiangsu Provincial Key Medical Center Foundation, and Jiangsu Provincial Medical Outstanding Talent Foundation.

Appendix A. Supplementary data

Supplementary data to this article can be found online at https://doi.org/10.1016/j.jare.2020.01.010.

References

[1] Murphy SV, Anthony A. 3D bioprinting of tissues and organs. Nat Biotechnol 2014;32:773–85.
[2] Campbell PG, Weiss LE. Tissue engineering with the aid of inkjet printers. Expert Opin Biol Ther 2007;7:1123–7.
[3] Mironov V, Kasyanov V, Markwald RR. Organ printing: from bioprinter to organ biofabrication line. Curr Opin Biotechnol 2011;22:667–73.
[4] Di Bella C, Duchi S, O'Connell CD, Blanchard R, Augustine C, Yue Z, et al. In situ handheld three-dimensional bioprinting for cartilage regeneration. J Tissue Eng Regener Med 2018;12:611–21.
[5] Singh S, Choudhury D, Yu F, Mironov V, Naing MW. In situ bioprinting - Bioprinting from benchside to bedside? Acta Biomater 2019.
[6] Keriquel V, Oliveira H, Remy M, Ziane S, Delmond S, Rousseau B, et al. In situ printing of mesenchymal stromal cells, by laser-assisted bioprinting, for in vivo bone regeneration applications. Sci Rep 2017;7:1778.
[7] Cohen DL, Lipton JI, Bonassar LJ, Lipson H. Additive manufacturing for in situ repair of osteochondral defects. Biofabrication 2010;2:035004.
[8] Lipskas J, Deep K, Yao W. Robotic-Assisted 3D Bio-printing for Repairing Bone and Cartilage Defects through a Minimally Invasive Approach. Sci Rep 2019;9:3746.
[9] Skardal A, Mack D, Kapetanovic E, Atala A, Jackson JD, Yoo J, et al. Bioprinted amniotic fluid-derived stem cells accelerate healing of large skin wounds. Stem Cells Transl Med 2012;1:792–802.
[10] Albanna M, Binder KW, Murphy SV, Kim J, Qasem SA, Zhao W, et al. In Situ Bioprinting of Autologous Skin Cells Accelerates Wound Healing of Extensive Excisional Full-Thickness Wounds. Sci Rep 2019;9:1856.
[11] O'Connell CD, Di Bella C, Thompson F, Augustine C, Beirne S, Cornock R, et al. Development of the Biopen: a handheld device for surgical printing of adipose stem cells at a chondral wound site. Biofabrication 2016;8:015019.
[12] Duchi S, Onofrillo C, O'Connell CD, Blanchard R, Augustine C, Quigley AF, et al. Handheld Co-Axial Bioprinting: Application to in situ surgical cartilage repair. Sci Rep 2017;7:5837.
[13] Li L, Yu F, Shi J, Shen S, Teng H, Yang J, et al. In situ repair of bone and cartilage defects using 3D scanning and 3D printing. Sci Rep 2017;7:9416.
[14] Mouser VH, Abbadessa A, Levato R, Hennink WE, Vermonden T, Gawlitta D, et al. Development of a thermosensitive HAMA-containing bio-ink for the fabrication of composite cartilage repair constructs. Biofabrication 2017;9:015026.
[15] Abbadessa A, Mouser VHM, Blokzijl MM, Gawlitta D, Dhert WJA, Hennink WE, et al. A Synthetic Thermosensitive Hydrogel for Cartilage Bioprinting and Its Biofunctionalization with Polysaccharides. Biomacromolecules 2016;17:2137–47.
[16] Sun W, Xue B, Ying L, Meng Q, Wei W. Polymer-Supramolecular Polymer Double-Network Hydrogel. Adv Funct Mater 2016. doi: https://doi.org/10.1002/adfm.201603512.
[17] Wang J, Zhang F, Tsang WP, Wan C, Wu C. Fabrication of injectable high strength hydrogel based on 4-arm star PEG for cartilage tissue engineering. Biomaterials 2017;120:11–21.
[18] Loebel C, Rodell CB, Chen MH, Burdick JA. Shear-thinning and self-healing hydrogels as injectable therapeutics and for 3D-printing. Nat Protoc 2017;12:1521–41.
[19] Jin J, Gans N. Parameter identification for industrial robots with a fast and robust trajectory design approach. Robotics Comput Integr Manuf 2015;31:21–9.
[20] van den Borne MP, Raijmakers NJ, Vanlauwe J, Victor J, de Jong SN, Bellemans J, et al. International Cartilage Repair Society (ICRS) and Oswestry macroscopic cartilage evaluation scores validated for use in Autologous Chondrocyte Implantation (ACI) and microfracture. Osteoarthr Cartil 2007;15:1397–402.
[21] Zhang K, Zhang Y, Yan S, Gong L, Wang J, Chen X, et al. Repair of an articular cartilage defect using adipose-derived stem cells loaded on a polyelectrolyte complex scaffold based on poly(l-glutamic acid) and chitosan. Acta Biomater 2013;9:7276–88.
[22] O'Driscoll SW, Keeley FW, Salter RB. Durability of regenerated articular cartilage produced by free autogenous periosteal grafts in major full-thickness defects in joint surfaces under the influence of continuous passive motion. A follow-up report at one year. J Bone Joint Surg Am 1988;70:595–606.
[23] McAlindon TE, Bannuru RR, Sullivan MC, Arden NK, Berenbaum F, Bierma-Zeinstra SM, et al. OARSI guidelines for the non-surgical management of knee osteoarthritis. Osteoarthritis Cartil 2014;22:363–88.
[24] Zhang W, Moskowitz RW, Nuki G, Abramson S, Altman RD, Arden N, et al. OARSI recommendations for the management of hip and knee osteoarthritis, Part II: OARSI evidence-based, expert consensus guidelines. Osteoarthritis Cartil 2008;16:137–62.
[25] Kunz M, Waldman SD, Rudan JF, Bardana DD, Stewart AJ. Computer-assisted mosaic arthroplasty using patient-specific instrument guides. Knee Surg Sports Traumatol Arthrosc Official J ESSKA 2012;20:857–61.
[26] Hangody L, Vasarhelyi G, Hangody LR, Sukosd Z, Tibay G, Bartha L, et al. Autologous osteochondral grafting–technique and long-term results. Injury 2008;39(Suppl 1):S32–9.
[27] Koh JL, Wirsing K, Lautenschlager E, Zhang LO. The effect of graft height mismatch on contact pressure following osteochondral grafting: a biomechanical study. Am J Sports Med 2004;32:317–20.
[28] Theissen NA, Laspas T, Archenti A. Closed-force-loop elastostatic calibration of serial articulated robots. Rob Comput Integr Manuf 2019;57:86–91.
[29] Lin H, Sun L. Searching globally optimal parameter sequence for defeating Runge phenomenon by immunity genetic algorithm. Appl Math Comput 2015;264:85–98.
[30] Ge Z, Li C, Heng BC, Cao G, Yang Z. Functional biomaterials for cartilage regeneration. J Biomed Mater Res Part A 2012;100:2526–36.
[31] Burdick JA, Prestwich GD. Hyaluronic acid hydrogels for biomedical applications. Adv Mater 2011;23:H41–56.
[32] Hangody L, Rathonyi GK, Duska Z, Vasarhelyi G, Fules P, Modis L. Autologous osteochondral mosaicplasty. Surgical technique. J Bone Joint Surg Am 2004;86-A(Suppl 1):65–72.